A 2D NUMERICAL MODEL OF ULTRASONIC WAVE PROPAGATION IN WOODEN UTILITY POLES USING EMBEDDED WAVEGUIDE EXCITATION TECHNIQUE

Yishi Lee*†

PhD Candidate
E-mail: yishi.lee@du.edu

Mohammad Mahoor

Professor
Ritchie School of Engineering and Computer Science
University of Denver
Denver, CO
E-mail: mohammad.mahoor@du.edu

Wayne Hall

President
Utility Asset Management Inc.
Denver, CO
E-mail: WayneHall@utilityassetmanagement.com

Abstract. Embedded waveguide technique is often not considered as a method for introducing ultrasonic wave for nondestructive testing (NDT). Because of the unique surface condition of wooden utility poles, the rough and uneven surface between the medium and the sensor introduces variation and signal attenuation, which impedes the use of a contact-based ultrasonic sensor. Many inspection and utility firms have adopted the use of inserting a small nail into the wooden pole for NDT. The mechanisms of excitation and reception of ultrasonic wave, however, are very different from the traditional contact-based mounting technique. Because very little research has been carried out on this methodology, this study focuses on the understanding of embedded waveguide excitation and reception in the time domain for wooden structure assessment in cylindrical symmetry. The resulted time domain waveform response is analyzed, and the associated findings will help infer important structural condition for NDT assessments. The study consists of numerical and empirical results to validate and understand the waveform characteristics and the associated energy modes that exist (Bodig 1982) in the two-dimensional wave propagation in a boundary medium.

Keywords: Embedded waveguide, Rayleigh wave excitation, elastodynamics in wood, wooden utility pole inspections.

INTRODUCTION

In the United States, about 100 million wooden poles are used to support two of the most critical infrastructures: the power and the communication distribution networks. Their structural integrity poses a vital concern for the sustainability of the system. Its undeniable importance demands a rigorous life cycle monitoring program to prevent unexpected structural failure that could incur

costly unplanned maintenance and repair work (Bodig 1982). In 2013, data collected by the Oregon State University had suggested that the average service life of a wood pole is far beyond the initial estimate of 30-40 yr because of the improvement in the quality of wooden utility poles. Data even suggested that an average pole service life could easily reach 80 yr in many areas (Morrell 2008). The current inspection process for determining a pole condition still results in that over a third of removed poles are deemed to be in good structural health for service. This conclusion suggests inadequacies in the current

---

* Corresponding author
† SWST member

inspection and demands an improved assessment process with better accuracy and consistency. One of the most critical areas for inspection is the ground line (GL) region, a few inches above the ground. This region experiences the most load condition while the environment is prone to different decays and the growth of fungi. Current techniques of inspecting the GL region rely on drilling and resistance microdrilling (Morrell 1996; Bhuyan 1998). Although it is a direct method of assessing the internal condition, the removal of material can inadvertently induce further damage by disturbing a previously established biological balance.

Nondestructive testing (NDT) using ultrasonic wave has been proven to be one of the most effective approaches to infer general wood quality and mechanical properties (Wang 2007). The time-of-flight (TOF) measurement is a typical method to assess wood quality by determining the time difference between the moments of transmission and the first detectable wave front. If a void or a significant decay exists internally along the path, the elastic wave will tend to propagate at a slower speed, resulting in a longer TOF (Wang et al 2004). In turn, it suggests the presence of decay. However, wood is classified as an orthotropic material with a complex internal structure, and wave propagation in such a nonlinear medium creates complicated temporal and spectral responses in different wave modes. Using TOF based on the initial arrival wave front as a sole indicator could result in erroneous and misleading property predictions. The time domain analysis into the received waveform can also infer more detail information that a single TOF cannot provide. Henceforth, it demands a realistic and complete understanding of wave propagation at the GL region.

To introduce ultrasonic wave into the medium, one of the techniques is to directly hammer a small waveguide into a specimen, creating about 1 cm insertion with a 4 mm diameter. An ultrasonic transducer as a load source is then mounted to the back to generate oscillating stress. The advantage of this approach over the traditional surface-mount sensor is to allow wave disturbance to be guided deep into the specimen while eliminating any surface variations. This study will also demonstrate the excitation of surface wave propagation at

the half-space boundary to enhance shell region condition assessment. Many utility firms have accepted such a small insertion technique as a nondestructive mounting technique. This simple application of introducing ultrasonic wave has been adaptive by several inspection firms such as the Utility Asset Management, Inc. (UAM).

Despite the advantage of this approach, the study of embedded waveguide radiation and the subsequent propagation and reception have not been previously investigated. Hence, this study focuses on the radiation pattern from an embedded waveguide excitation, propagation of the elastic wave in the orthotropic medium, and the reception of the elastic wave using the same embedded waveguide. This study offers the latest finite element model of wood poles by extending the previous work carried out by (Ting 1996; Payton 2003; Senalik 2013). The result will be validated through empirical data obtained using the latest commercially deployed NDT device UB1000 developed jointly by Utility Asset Management Inc. (Denver, CO) and University of Denver (Denver, CO).

MATERIALS AND METHODS

To analyze the response obtained by using the embedded waveguide excitation technique, a numerical model is first created using the finite element method (FEM) based on the FEM-based COMSOL Multiphysics software (developed by COMSOL Group, Stockholm, Sweden). We will discuss the detail configurations of the numerical model. Using a new utility pole specimen, we will discuss the preparation and experimental procedures for deploying the UB1000 device. The empirical and numerical results will be compared to help validate the numerical model.

Numerical Approach

Acoustic propagation at the GL region is an elastodynamic problem with the cylindrical symmetry. To simulate ultrasonic wave propagation in the time domain, a numerical model based on the FEM provides the flexibility to understand the physical phenomena in complex geometries. The simulation environment is discussed through

the following areas: the overall governing equation, initial and boundary conditions, mechanical properties of the medium, discretization and mesh size, and time stepping selection.

The governing equation of the model. Based on the classical elastodynamic radiation formulation with a body force, the classical non-homogenous wave equation models the elastic wave propagation. The time domain expression is written as follows:

$$C_{ijkl}u_{k,lj} = \rho\ddot{u}_i - \sigma_{ij}, \qquad (1)$$

where $\ddot{u}$ denotes the second time derivative of the displacement field u, and it is often decomposed into the longitudinal and transverse potential fields through the Helmholtz decomposition (Achenbach 2012). In the two-dimensional case, the stiffness matrix C_{ijkl} describing an orthotropic medium in the cylindrical coordinate system is expressed as follows:

$$C = \begin{bmatrix} c_{11} & c_{12} & 0 \\ c_{21} & c_{22} & 0 \\ 0 & 0 & c_{33} \end{bmatrix}, \qquad (2)$$

with $c_{11} = 1/E_R$, $c_{12} = c_{21} = -v_{TR}/E_T$, $c_{22} = -1/E_T$ and $c_{33} = 1/G_{TL}$, where E_R and E_T are the Young moduli in the radial (R) and tangential (T) directions, $\nu_{i,j}$ corresponds to the Poisson's ratios with the longitudinal deformation in the direction of stress i and shear deformation in the j direction, and G_{ij} are the shear moduli. The entries in the stiffness matrix are the functions of the mechanical properties. US Department of Agriculture has compiled a comprehensive database (Taggart 1999) detailing the mechanical properties needed for the simulation. Four commonly known species used in the utility pole industry are the western red cedar, Douglas-fir, ponderosa, and red pine. Using the definition for the entries of the stiffness matrix (2), Table 1 shows calculated values for off-diagonal entries c_{12} and c_{21}. The similar magnitudes in the off-diagonal elements help validate the assumed orthotropic properties.

The transient response of an elastic waveguide embedded in a wood specimen represents the

Table 1. Cell values of different species, unit: $\times 10^{-10}$ Pa^{-1}.

	c_{11}	c_{22}	c_{12}	c_{21}	c_{33}
Douglas-fir	11.7	15.9	5.94	4.55	113
Red cedar	19.1	26	10.5	9.24	186
Red pine	13.1	17.9	5.5	5.36	128
White spruce	14.9	2.02	4.95	6.46	144

body force f. At the initial time $t = 0$, the transient load is exerted on the waveguide through the excitation interface shown in Fig 1. A classical description of transient longitudinal wave propagation of a piezoelectric transducer is modeled as follows (Cochran 2012):

$$\sigma_{rr}(x = b) = \sigma_0 e^{-\alpha(t - t_c)^2} e^{i\omega t}, \qquad (3)$$

where σ_0 is the amplitude, ω is the resonant frequency of the oscillating piezoelectric material, α represents the bandwidth, and t_c is a constant denoting the time when the maximum amplitude occurs.

To discretize the governing partial differential eq 1 to be suitable for FEM, the method of lines can be deployed, transforming spatial derivatives using the finite difference equation. The resulted equation is commonly known as the semiexplicit differential algebraic equation (DAE). The wide occurrence of DAE in many scientific and engineering applications has piqued many interests to develop the appropriate numerical solvers. The backward differentiation formula (BDF) has known to be one of the most versatile and popular numerical technique. Hence, it is used in this problem (Brenan et al 1996).
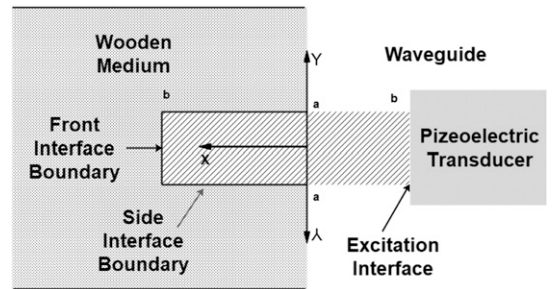

Figure 1. Geometry of inserted waveguide.

Boundary condition. By imposing the longitudinal wave propagation in the axial direction along the waveguide and the interface traction condition, as the longitudinal mode propagates along the body of the waveguide, we consider the wave interaction with the front and the side interfaces. Because the front interface boundary is perpendicular to the direction of wave propagation, we can neglect any mode conversion and only consider the longitudinal wave mode. Based on the theoretical piezoelectric response from (3), using notations from Fig 1, it yields the following equation:

$$\sigma_{rr|r=b} = \sigma_0 e^{-\alpha(t-t_c)^2} e^{i(kb-\omega t)} \quad \text{for } |\theta| \le a, \tag{4}$$

where k is the wave number. For side interface boundary parallel to the wave propagation, total mode conversion transforms longitudinal wave into the shear wave. By imposing the same forcing term (3) for the waveguide, it yields the side interface boundary condition as follows:

$$\sigma_{\theta r|\theta=\pm a} = \sigma_0 e^{-\alpha(t-t_c)^2} e^{i(qr-\omega t)} \quad \text{for } 0 \le r \le a, \tag{5}$$

where q is the wave number associated with the shear wave. At the half-space of a utility pole at the GL, the boundary condition along the circumference of the cross-section can be reasonably assumed to have zero longitudinal and shear stresses, which can be given by the following equation:

$$\sigma_{rr} = 0, \quad \sigma_{\theta r} = 0. \tag{6}$$

Mesh element size. Because of the complex microscopic structure of the wood cells, there is a significant difference between the microscopic and macroscopic/effective properties. Each element in a mesh must reflect macroscopic mechanical properties. A classical view of a wood cell is often considered to be in a honeycomb-like structure. By using the computational upscaling technique (Guedes and Kikuchi 1990), the microscopic properties can converge to the macroscopic properties by simply replicating a single cell to a multicell structure as shown in Fig 2. Figure 3 represents the largest dimension of the multiscale structure in the x-axis. The y-axis represents the ratio between the microscopic properties p and the macroscopic properties p_c. The convergence of the Young's modulus in the radio and tangential directions, Poisson's ratio, and the shear modulus converge at approximately 1 mm, which represents the minimum element size needed to allow macroscopic effective properties to be used for an accurate solution.

The second factor is aliasing in resolving the waveform. Wavelength λ is defined by the phase speed and the frequency of a traveling wave. In porous material, the longitudinal and transverse speeds are expressed as follows:

$$v_L^2 = \frac{3K^* + 4G^*}{3\rho^*} \quad \text{and} \quad v_T^2 = \frac{G^*}{\rho^*}, \tag{7}$$

where the superscript * denotes the effective properties, subscripts L and T signify the longitudinal and transverse wave, respectively, G is the shear modulus, K is the bulk modulus, and ρ^* is the average density expressed as follows:

$$\rho^* = \rho_w(1-\phi), \tag{8}$$

where ρ_w is the cell wall density and ϕ is the porosity. This value depends on the species and the time of the year, but it is typical to estimate the ratio of 20-50% (Cown 1975).
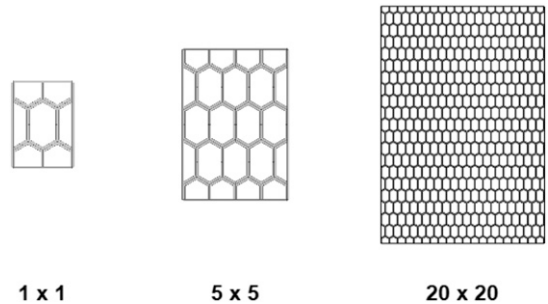

1 x 1   5 x 5   20 x 20

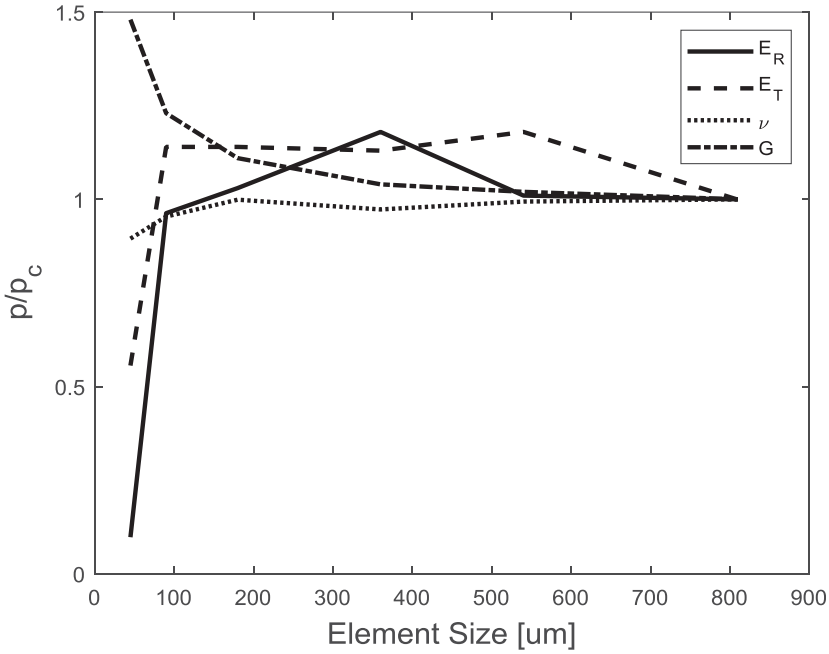Figure 2.   Replication of the single wood fiber cell structure.

Figure 3.   Homogeneity and convergence of physical properties for Douglas-fir.

To resolve the shortest wavelength $\lambda_{\min}$, recall $\lambda_{\min} = v_{\min}/f_0$. It is noted that $v_T > v_L$ (Rose 2004) and having $v_{\min} = v_L$, it yields the following:

$$\lambda_{\min} = \frac{1}{f_0 \rho^{1/2}} \left(\frac{G^*}{1 - \phi} \right)^{1/2}. \qquad (9)$$

According to the Nyquist–Shannon sampling theory, the smallest element size needs to be at least half of the $\lambda_{\min}$. Table 2 shows a typical softwood used in the utility industry and the recommended mesh sizes.

Time step selection. To determine an appropriate time step, the first criterion is the aliasing due to a low sampling rate. The excitation of the ultrasonic wave has a center frequency f_c of

Table 2.   Maximum element size for different species.

	Maximum element size (μm)
Douglas-fir	613
Red cedar	361
Red pine	702
White spruce	663

50 kHz. According to the Nyquist–Shannon sampling theorem, the sampling frequency needs to be at least two times the center frequency. Hence, to resolve a proper waveform, the upper limit for dt was chosen to be 10 times greater than f_c, resulting in a time step of 1×10^{-6} s.

The second criterion is to control the truncation error and the interpolation error due to the numerical method, stability, and convergence of the iterative technique. For anisotropic wave equation with nonlinear terms, the issue of the stiffness in the partial differential equation (PDE) arises, which demands a numerical technique that is more resistant to numerical instability (Kassam and Trefethen 2005). To determine a proper time stepping, the local relative errors can be observed by comparing the predicted values and the approximated value at every step. According to (Brenan et al 1996), a relative error is as follows:

$$\text{ERR} = M \left| \left| u_{n+1} - u_{n+1}^0 \right| \right| \leq 1.0 \qquad (10)$$

where u_{n+1}^0 is the vector containing all the predicted values based on the predictor formula (Krogh 1974) and u_{n+1} contains the approximated

values. $||\cdot||$ denotes the L_2 norm. M is a coefficient related to a chosen step size. Based on (10), Fig 4 shows the relative error using different step sizes. Although small step sizes provide a better temporal resolution, it increases computational time. As illustrated in Fig 5, the diminishing in return helps justify an efficient time step, and yet, it still achieves accurate results.

Empirical Approach

To ensure the results can be compared, it is essential to mitigate variations between the empirical and numerical approaches. Hence, a healthy pole will be used to ensure that all the desired mechanical properties are intact. The embedded waveguides are inserted in accordance with the configuration of the numerical model.

Preparation and procedures. At the 32-inch circumference of the new pretreated Douglas-firs wooden pole, the test configuration of using a pair of UB1000 units with the embedded waveguides
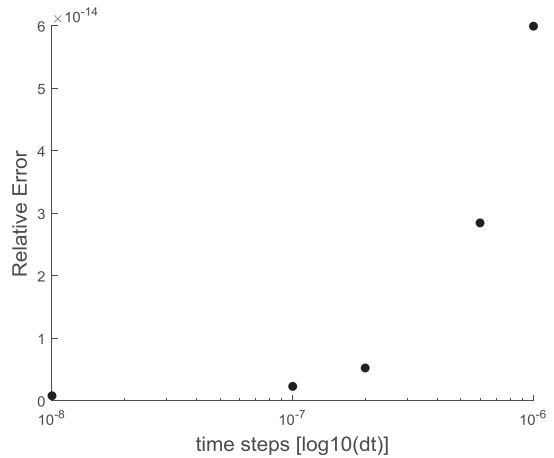
Figure 5.   Relative error of different step sizes.

is shown in Fig 6(c). For the experiment, a pair of transmitting and receiving wireless ultrasonic transducer UB1000s was used. Figure 6(b) shows a UB1000 unit with a waveguide mounted at the front of the transducer horn. The system consists of an ultrasonic transducer assembly that can
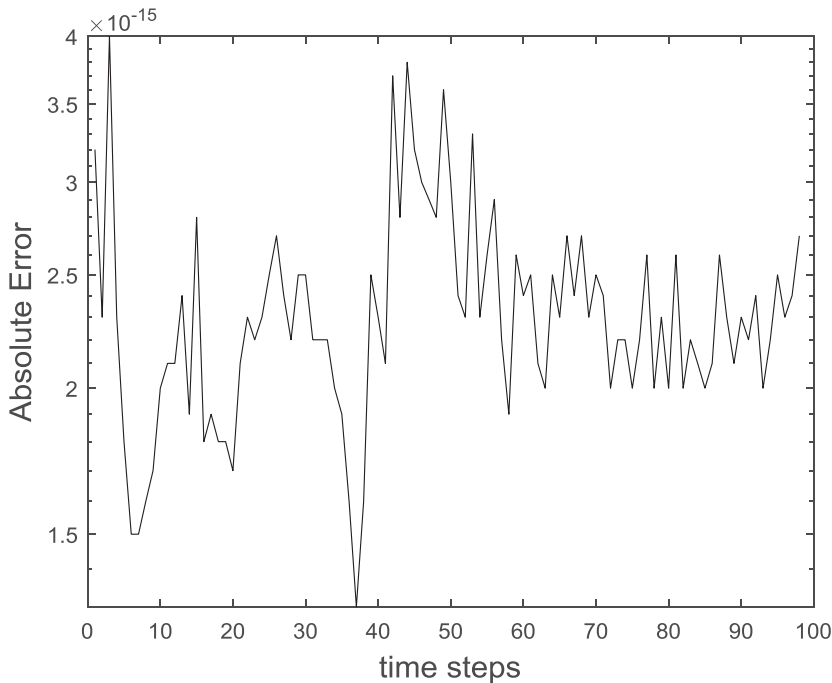
Figure 4.   Nearly random oscillation suggests the stability of the deployed numerical solver.
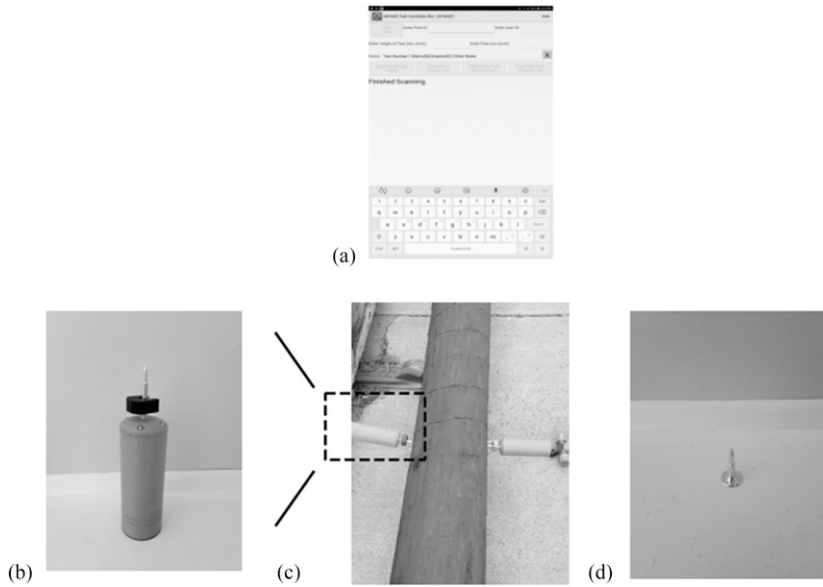
Figure 6. Equipment required for the experiment. (a) UB1000 Command GUI, (b) wireless UB1000 probe with the waveguide mounted, (c) test configuration, and (d) embedded waveguide.

bidirectionally convert between the mechanical and electrical energies. A custom-designed printed circuit assembly (PCA) is used to generate modulated excitation voltage and acquire condition and convert received wave energy into a digital signal. The unit is commanded remotely and wirelessly with a SAMSUNG galaxy Tablet (Samsung Group, Samsung Town, Seoul, South Korea) via the Bluetooth interface protocol. This system allows the users to command, receive, and process diagnostic waveforms to help analyze the structural condition. A separate design study was conducted to find an optimal waveguide for this application (illustrated in Fig 6[d]). Because of the proprietary and the patentability nature of this part, we will not further discuss the details of the waveguide design.

To perform a diagnostic assessment, two aluminum waveguides are inserted into the medium at the opposite ends. The depth of insertion is about 1.3 cm below the surface. Threaded transducer horns are mounted to the waveguide excitation interface using a custom-designed mounting coupler as shown in Fig 6(b). Using a tablet with the UB1000 application (shown in Fig 6[a]) installed, an initiation command is sent to both units to initiate probe synchronization. Once completed, a high voltage square pulse is transmitted to the transducer input to excite the piezoelectric material at its resonant frequency. The generated stress wave propagates through the transducer front mass (horn and waveguide) and into the medium. In the meanwhile, the receiving probe continues listening for any disturbances from the medium. Through the UB1000 application, the conditioned waveforms are transmitted to the tablet wirelessly.

RESULTS AND DISCUSSION

The wave propagation mechanism will be discussed next with emphasis on the time and frequency domain responses at the receiving waveguide. The numerical results will be compared directly with the empirical data to help infer critical characteristics in wave propagation in a wooden pole.

Numerical Results

Using Douglas-firs as an example and the described model configuration, this section analyzes the results produced by the COMSOL FEM

model using the BDF solver. The analysis focuses on three characteristics: radiation of the ultrasonic wave, its propagation, and the reception.

Radiation through interfaces. The waveguide consists of the front interface and the side interface. At the front interface because of the imposition of external disturbance according to (4) and the assumed longitudinal wave mode, we see the longitudinal wave is the primary mode of propagation. Because of the dissimilar material, a portion of wave energy transmitted into the immediate medium. The unbounded space causes the wave front to expand outward. The orthotropy in the tangential and longitudinal directions generates a beam profile that
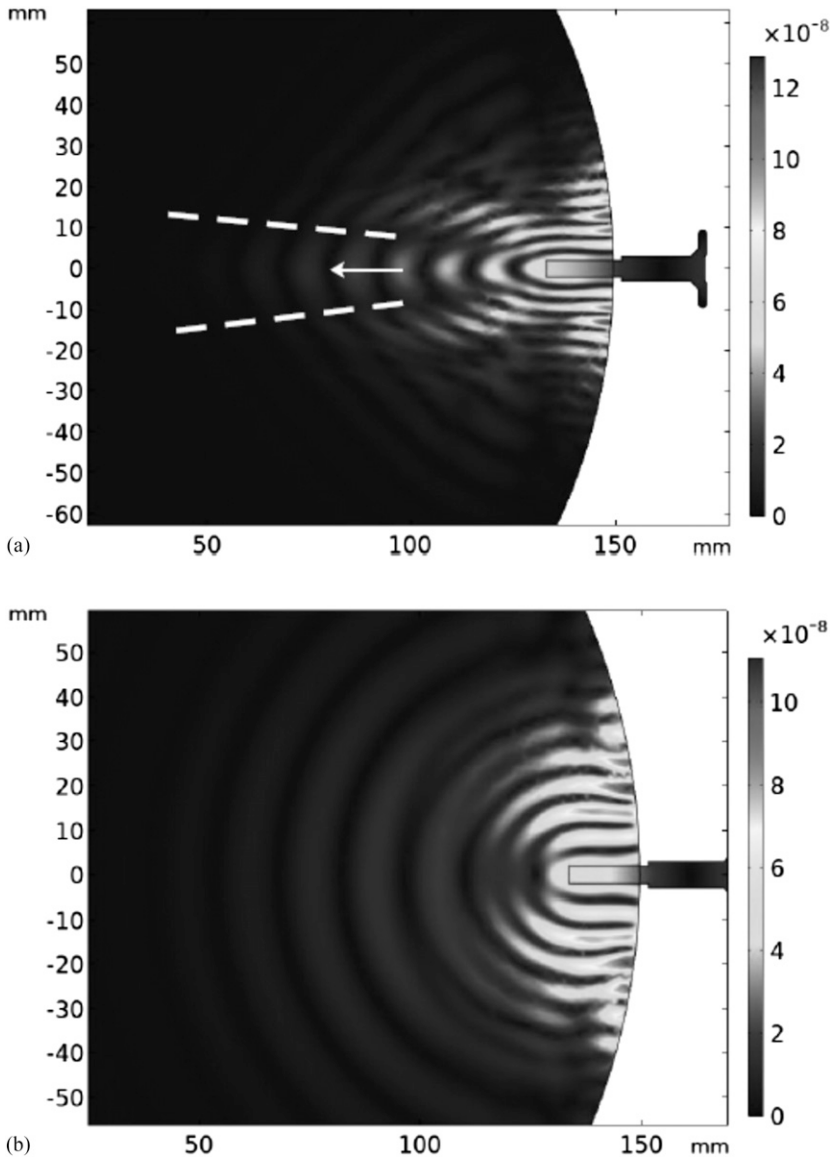

Figure 7. Magnitude of the displacement fields at (a) orthotropic medium where the dotted white lines denote the beam width boundary and the white arrow denotes the energy vector and (b) isotropic medium using average properties.
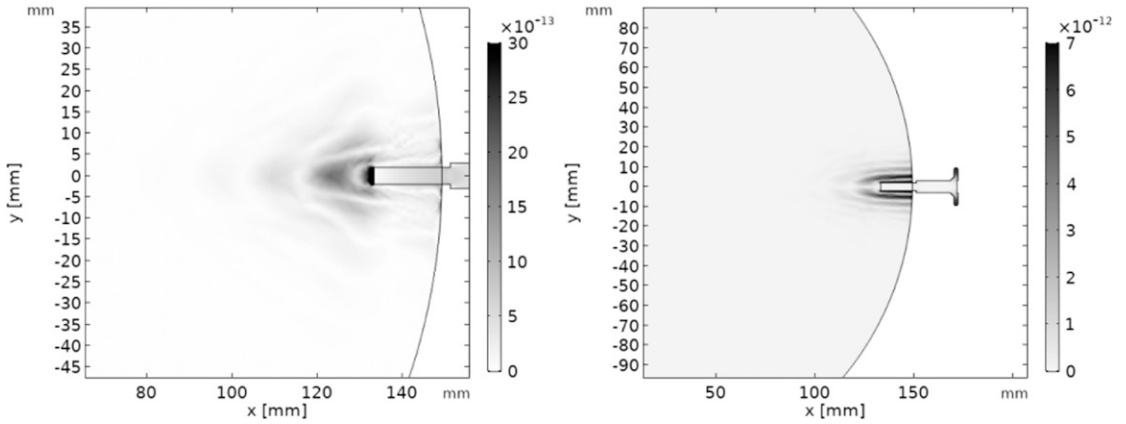
Figure 8.   The radiation pattern of the longitudinal displacement field on the left and the transverse displacement field on the right at t = 80 μs.

was previously predicted by (Rose 2004). A comparative plot shown in Fig 7(a) illustrates a pronounced beam profile because of the inhomogeneous wave front and a uniform wave front formed under the isotropic medium illustrated in Fig 7(b).

Along the side interface, the combined traction condition and the assumed longitudinal mode generates longitudinal oscillation along that interface. This oscillation in the *x*-direction at the interface excites the so-called Rayleigh wave (Rayleigh 1885) mode that propagates in the *y*-direction or the curved half-space boundary. According to (Viktorov 1967), in the curved half-space, Rayleigh wave mode consists of both the longitudinal displacement field ϕ and the transverse displacement field ψ, which can be given by the following equation:

$$\begin{aligned} \phi &= A e^{ip\theta} I_p(k_l r); \\ \psi &= B e^{ip\theta} I_p(k_t r), \end{aligned} \quad (11)$$

where A and B are the amplitudes, I_p is the Bessel function of an order p, where p is the angular wave number expressed as $2\pi R/\lambda$, θ is the tangential direction, and k_l and k_t are the wave numbers for the longitudinal and tangential wave numbers, respectively, expressed as $k = 2\pi/\lambda$.

The inhomogeneous Rayleigh wave contains two fundamental modes: longitudinal and transverse wave with identical wave number p.

At $t = 80$ μs, both the transverse wave mode ψ and the longitudinal wave mode ϕ propagate along the half-space boundary, which can be noted in Fig 8.

Propagation. The longitudinal and transverse wave propagations in the wooden medium at different times are illustrated in Fig 9. At $t = 150$ μs, the darkest region suggests a stronger longitudinal wave energy near the front interface, whereas the transverse wave mode mainly resides near the side interface. Near the side interface, the transverse component is stronger than the longitudinal component. At $t = 200$ μs, the longitudinal wave from the front interface continues propagating outward, generating a pronounced "arrow-like" wave front as a result of the orthotropy of the material. Simultaneously, two packets of the Rayleigh wave energy propagating along the half-space boundary in the opposite directions with the same angular wave speed agree with the identical wave number predicted by (11). At $t = 300$ μs, the longitudinal wave front traveling in the radial direction intercepts the center and induces the radial wave expanding outward. As the energy of the longitudinal mode intensifies, it appears to be "deflected" into two different wave packets propagating at a slower speed (circled in black). The resulted wave front from this model qualitatively agrees with other
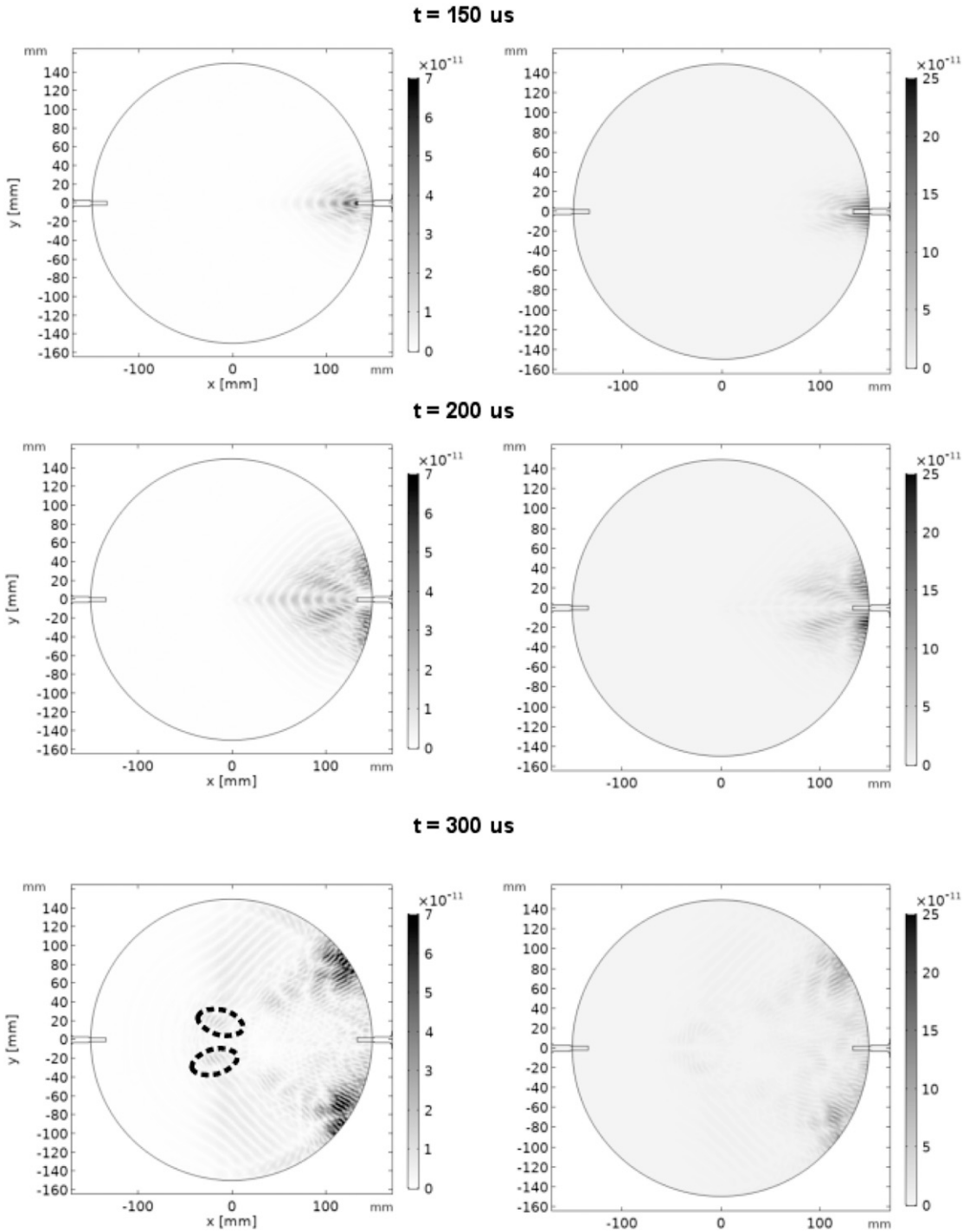
Figure 9.   Time elapse of wave propagation. Column 1 illustrates the longitudinal wave propagation and column 2 illustrates the transverse wave propagation.

models (Senalik 2013) and gives additional details about the emitting beam profile and the full waveform propagation.

Reception. When incoming wave envelops reach the receiving waveguide, the waveforms interact with the embedded portion of the waveguide before being guided to the excitation interface. Figure 10 shows a three-dimensional FEM waveguide model. The model imposes time-harmonic stress disturbance in the *x*-direction at the front end, side, and both interface boundaries to mimic an incoming wave envelope. The result is depicted on the right of the model. The solid line represents the side interface reception, the dotted line represents the front interface reception, and the dashed line represents incident waves at all interfaces. The strong time domain response describes the characteristics of waveguide reception capability, but more importantly, it suggests the retention of the initial waveform and the pronounced difference between incident wave at the front and side interfaces. By knowing the reception characteristics of the waveguide, Fig 11 shows the transmitted waveforms of the total displacement reaching the receiving waveguide. Figure 11(a) shows the radial incident wave initially emitted from the front end of the transmitting probe. This uniform and diffusive longitudinal incident wave reaches the front

aperture causing a pronounced initial wave envelop labeled as 1. The wave originated from the front aperture of the transmitting waveguide propagating outward. As it reaches the half-space boundary, reflection and mode conversion mechanisms cause the energy to focus at the receiving end, causing the second wave envelop. We labeled it as 2. The enhanced energy level suggests the wave interaction with the front and side interfaces. Finally, the strongest wave front labeled as 3 is the signature of the Rayleigh wave propagation that reaches the side interface of the receiving waveguide. The pronounced excitation produces an enhanced response in the time domain plot for the receiving probe. In Fig 11(a), t_1, t_2, and t_3 denote the times of energy peak in each wave mode.

Empirical vs Model Results

The model does not account for the following variations in the experiment. Because of the manufacturing process and wood poles were not cut into a perfect cylinder, a variation due to imperfect cylindrical symmetry produces a slight difference in wave trajectories. The initial MC of the wood pole was not considered in the model. In principle, moisture is a *dispersive* media creating energy attenuation with
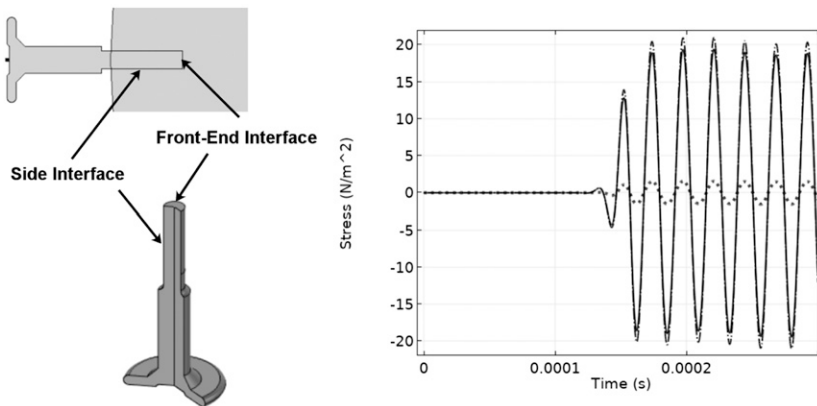

Figure 10.   Energy level of a wave incident at the front end (solid line) or the side (dotted line) and combined (dashed-dotted line).
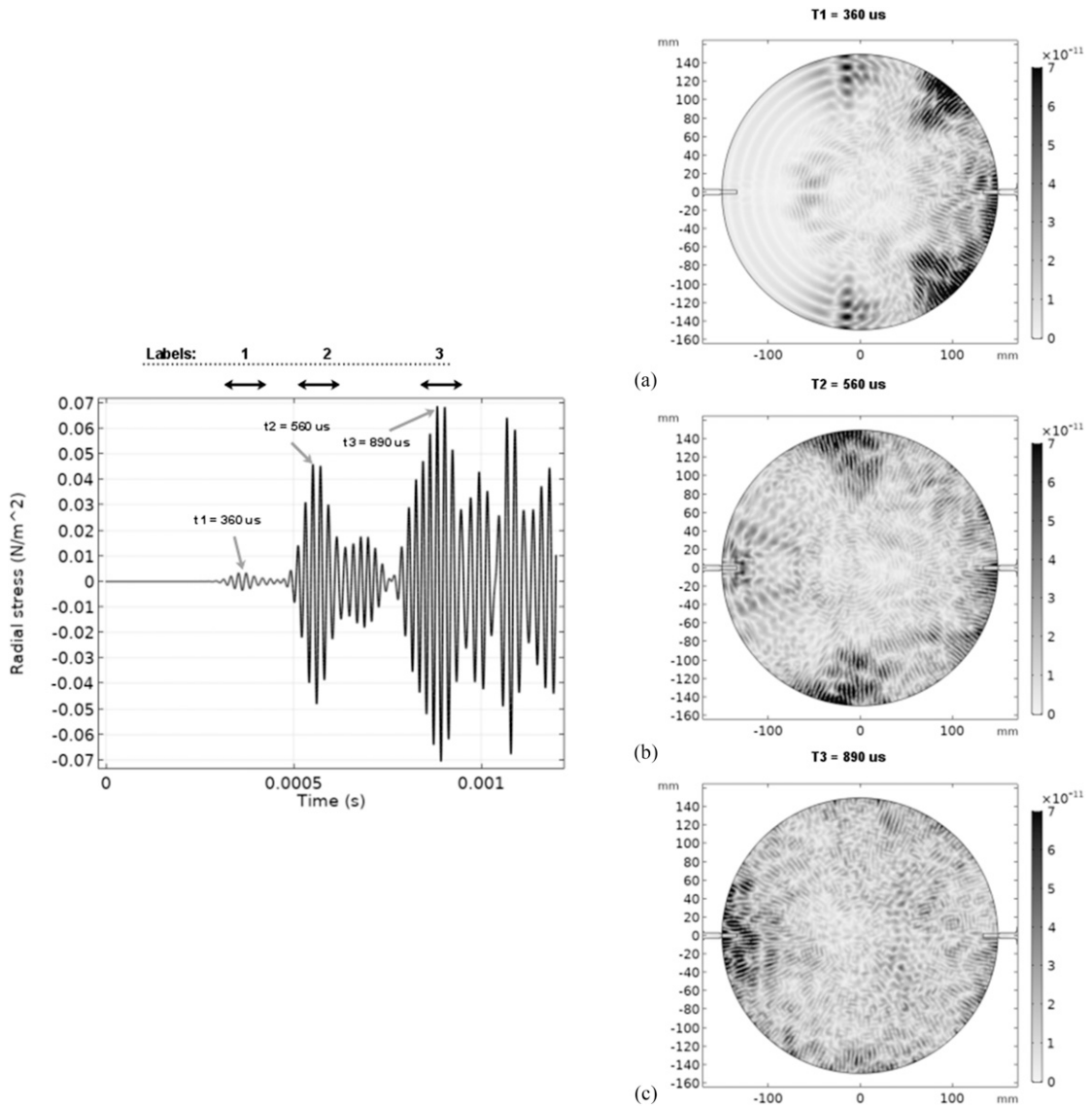
Figure 11.   Received time domain signal with the corresponding states of wave propagation at (a) $T = 360\ \mu s$, (b) $T = 560\ \mu s$, and (c) $T = 890\ \mu s$.

frequency dependency. In this study, narrow band ultrasonic wave centered at 50 kHz with a ± 5-kHz bandwidth is introduced; it is safe to assume that the attenuation is constant across the applied frequency band. Finally, the mounting interface between the transducer and the waveguide is not modeled. To validate the model, we perform the time and frequency domain comparison between the empirical and numerical results.

Time domain. Figure 12 shows the received filtered data represented in time. It depicts three distinct wave envelops with increasing amplitude. The result is similar to the numerical result, preliminarily suggesting the arrival wave fronts 1, 2, and 3. To confirm the identity of the wave envelopes 1, 2, and 3, we first perform time normalization with respect to the wave front 3. It is a technique to eliminate the unaccounted
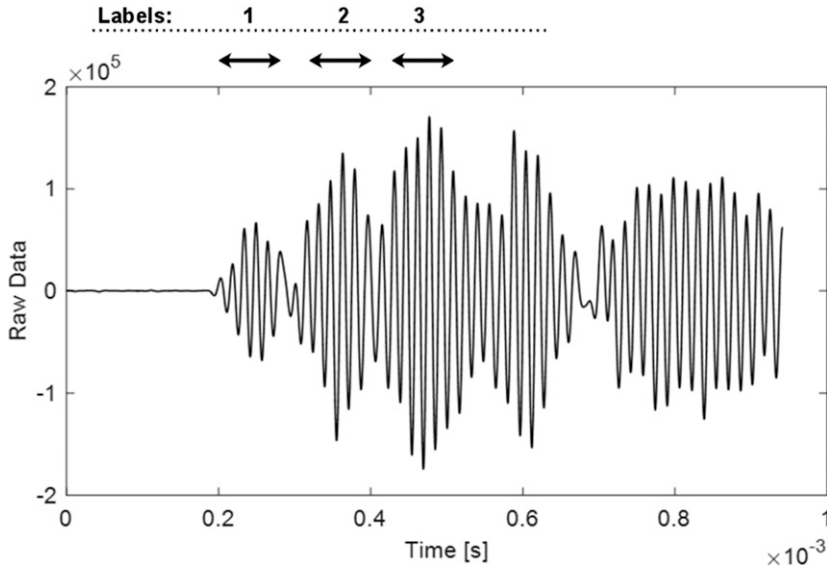
Figure 12.   Measured waveform obtained from UB1000.

differences in the actual mechanical properties and the assumed mechanical properties in the model. We then perform a correlation calculation among the normalized arrival wave fronts using the Pearson correlation coefficient. By definition, it is to measure the relationships between two random variables (Benesty 2009), which can be given by the following equation:

$$\rho(x_m, x_e) = \frac{E(x_m x_e)}{\sigma_{x_m} \sigma_{x_e}},$$

where $E(x_m x_e)$ is the cross-correlation between the random variables for the model data x_m and empirical data x_e, respectively. σ_{x_m} and σ_{x_e} are variances of the model and empirical data, respectively. The result described in Table 3 shows the Pearson correlation coefficient to be 0.98, suggesting that the time wave fronts 1, 2, and 3 of the empirical and numerical results are closely related.

Frequency domain. Using Fourier transformation, spectral information in envelops 1 and 3 is illustrated in Fig 13. The top plot group depicts the empirical result obtained from the UB1000 system. The frequency responses from each envelop 1 and 3 are analyzed. Table A in Fig 13 shows that the frequency between 1 and 3 are virtually identical, despite the difference in propagation. Table B in Fig 13 agrees with the empirical results but with a slight shift of frequency of 1 kHz. The shift in frequency is partially due to the resonant frequency of the transducers and the mounting mechanisms not being modeled in the simulation.

SUMMARY AND CONCLUSIONS

This study has investigated the radiation, propagation, and reception characteristics of using an embedded waveguide to introduce and receive elastic waves at the GL region. A brief comparative study shows that the model agrees with other

Table 3.   Correlation of the model and empirical data.

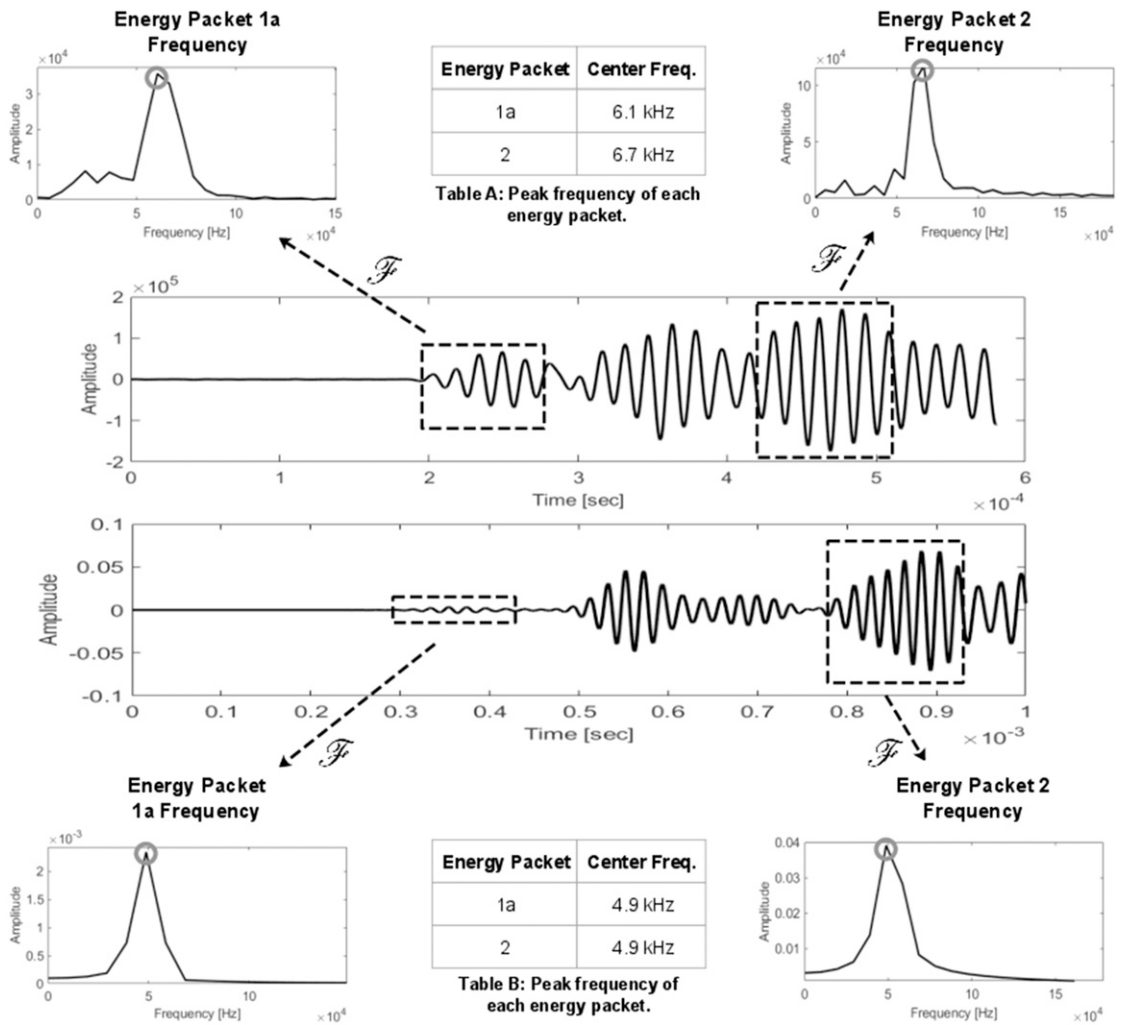|	Simulation result		Empirical result		Difference in normalized values	Pearson correlation coefficient
	Time	Normalized	Time	Normalized		
1st peak	0.36	0.4	0.24	0.5	20%	$R^2 = 0.98$
2nd peak	0.56	0.63	0.36	0.75	16%	
3rd peak	0.89	1	0.48	1	n/a	

Figure 13.   Spectral graph of the energy packet 1A and 2.

previous models with more detail features. Simulated waveforms from the latest numerical model suggest a spatial dispersion of three different wave envelops due to the waveguide/medium interfaces. Subsequent empirical data using the UB1000 ultrasonic device further validate the accuracy of the model. More importantly, it qualitatively agrees with the numerical results by exhibiting the same time domain characteristics.

REFERENCES

Achenbach J (2012) Wave propagation in elastic solids, Vol. 16. Elsevier, Amsterdam, The Netherlands.

Benesty J, Chen J, Huang Y, Cohen I (2009) Noise reduction in speech processing (Vol. 2). Springer Science & Business Media.

Bhuyan GS (1998, April) Condition based serviceability and reliability assessment of wood pole structures. Pages 333-

339 *in* ESMO'98-1998 IEEE 8th International Conference on Transmission and Distribution Construction, Operation and Live-Line Maintenance Proceedings ESMO'98 Proceedings. ESMO 98 The Power is in Your Hand. IEEE, Orlando, FL.

Bodig J, Phillips G, Goodman J, Landers P (1982) Reliability of wood transmission structures through nondestructive evaluation. IEEE Trans Power Apparatus System 8:2409-2414.

Brenan KE, Campbell SL, Petzold LR (1996) Numerical solution of initial-value problems in differential-algebraic equations, Vol. 14. Siam, Philadelphia, PA.

Cochran S (2012) Ultrasonic transducers. Elsevier, Amsterdam, The Netherlands.

Cown DJ (1975) Variation in tracheid dimensions in stem of a 26-year-old radiata pine tree. Appita 28(4):237-245.

Guedes J, Kikuchi N (1990) Preprocessing and postprocessing for materials based on the homogenization method with adaptive finite element methods. Comput Methods Appl Mech Eng 83:143-198.

Kassam A, Trefethen L (2005) Fourth-order time-stepping for stiff PDEs. SIAM J Sci Comput 26:1214-1233.

Krogh F (1974) Changing step size in the integration of differential equations using modified divided differences. Pages 22-71 *in* Proc. Conference on the Numerical Solution of Ordinary Differential Equations, October 1974, Springer, Berlin, Heidelberg.

Morrell JJ, Manual WPM (1996) Forest Research Laboratory, Oregon State University, Corvallis.

Morrell JJ (2008) Estimated service life of wood poles. Technical Bulletin, North American Wood Pole Council. pp. 1-5.

Payton R (2003) Wave fronts in wood. Q J Mech Appl Math 56(4):527-546.

Rayleigh L (1885) On waves propagated along the plane surface of an elastic solid. The London Mathematical Society, London, UK. pp. 4-11.

Rose J (2004) Ultrasonic waves in solid media. Cambridge University Press, Cambridge, United Kingdom.

Senalik A (2013) Detection and assessment of decay in wooden utility poles using an acoustic approach. Int J Environ Prot 3(8):13.

Taggart GL (1999) Rubrics: A handbook for construction and use. R&L Education, Lanham, MD. pp. 5-2-5-24.

Ting T (1996) Anisotropic elasticity: Theory and applications. Oxford Science Publications, New York, NY.

Viktorov I (1967) Rayleigh and lamb waves. Plenum, New York, NY.

Wang X, Divos F, Pilon C, Brashaw BK, Ross RJ (2004) Assessment of decay in standing timber using stress wave timing nondestructive evaluation tools: A guide for use and interpretation. Pages 1-12 *in* Gen. Tech. Rep. FPL-GTR-147. US Department of Agriculture, Forest Service, Forest Products Laboratory, Madison, WI, 147

Wang XC (2007) Acoustic assessment of wood quality of raw forest materials: A path to increased profitability. For Prod J 57(5):6-14.